


Large deviations of the interface height in the Golubović-Bruinsma model of stochastic growth

Baruch Meerson^{*} and Arkady Vilenkin[†]

Racah Institute of Physics, Hebrew University of Jerusalem, Jerusalem 91904, Israel

 (Received 15 March 2023; accepted 22 June 2023; published 18 July 2023)

We study large deviations of the one-point height H of a stochastic interface, governed by the Golubović-Bruinsma equation, $\partial_t h = -v\partial_x^4 h + (\lambda/2)(\partial_x h)^2 + \sqrt{D}\xi(x, t)$, where $h(x, t)$ is the interface height at point x and time t and $\xi(x, t)$ is the Gaussian white noise. The interface is initially flat, and H is defined by the relation $h(x = 0, t = T) = H$. We focus on the short-time limit, $T \ll T_{\text{NL}}$, where $T_{\text{NL}} = v^{5/7}(D\lambda^2)^{-4/7}$ is the characteristic nonlinear time of the system. In this limit *typical*, small fluctuations of H are unaffected by the nonlinear term, and they are Gaussian. However, the large-deviation tails of the probability distribution $\mathcal{P}(H, T)$ “feel” the nonlinearity already at short times, and they are non-Gaussian and asymmetric. We evaluate these tails using the optimal fluctuation method (OFM). The lower tail scales as $-\ln \mathcal{P}(H, T) \sim H^{5/2}/T^{1/2}$. It coincides with its analog for the Kardar-Parisi-Zhang (KPZ) equation, and we point out to the mechanism of this universality. The upper tail scales as $-\ln \mathcal{P}(H, T) \sim H^{11/6}/T^{5/6}$, it is different from the upper tail of the KPZ equation. We also compute the large deviation function of H numerically and verify our asymptotic results for the tails.

DOI: [10.1103/PhysRevE.108.014117](https://doi.org/10.1103/PhysRevE.108.014117)

I. INTRODUCTION

Stochastic growth models out of equilibrium have been at the forefront of nonequilibrium statistical physics since the early 1990s [1–3]. Probably the most celebrated paradigmatic model of this class is described by the Kardar-Parisi-Zhang (KPZ) equation. In one dimension, this equation has the form [4]

$$\partial_t h = v\partial_x^2 h + \frac{\lambda}{2}(\partial_x h)^2 + \sqrt{D}\xi(x, t), \quad (1)$$

where $h(x, t)$ is the height of a growing KPZ interface at the point x of a substrate at time t , and $\xi(x, t)$ is a Gaussian white noise with zero average and

$$\langle \xi(x_1, t_1)\xi(x_2, t_2) \rangle = \delta(x_1 - x_2)\delta(t_1 - t_2). \quad (2)$$

At late times, the lateral correlation length of an infinite one-dimensional KPZ interface grows as $t^{2/3}$, and the characteristic interface width grows as $t^{1/3}$. The exponents $2/3$ and $1/3$ are hallmarks of the KPZ universality class: an important universality class of non-equilibrium growth [1–9].

Since the early 2010s, more detailed characteristics of the height fluctuations of the KPZ interface have been introduced and studied. One of these characteristics is the probability distribution $\mathcal{P}(H, t)$ of the interface height at $x = 0$ at time t , $H = h(x = 0, t)$. This distribution strongly depends on the initial condition $h(x, t = 0)$ and, in an infinite system, this dependence persists forever [7–9]. There has been a spectacular progress in quantitative analysis of this problem. It started

from the discovery of remarkable exact representations for $\mathcal{P}(H, t)$ for several “standard” initial conditions and extraction of relevant asymptotics, see Refs. [7–9] for reviews. This line of work received the name “stochastic integrability.”

In parallel, the one-point height fluctuations have been studied by the optimal fluctuation method (OFM) [10–26]. The OFM (also known in other areas of physics and mathematics as the weak-noise theory, the instanton method, the dissipative WKB approximation, the macroscopic fluctuation theory, etc.) is an asymptotic method, based on a problem-specific small parameter. The method involves a saddle-point evaluation of the exact path integral for stochastic partial differential equations, including the KPZ equation. This is achieved via minimization of the proper action functional and determination of the optimal path of the system. In the context of surface growth in one dimension it is the most likely history of the interface $h(x, t)$, and the most likely realization of the noise $\xi(x, t)$, which dominate the contribution of different histories to a large deviation in question. It has been found that, at short times, the OFM captures the whole large-deviation function of H for a broad variety of initial and boundary conditions [10–26]. The optimal paths not only make it possible to evaluate the large-deviation function of H but also provide a useful insight into physics of large deviations. For some initial conditions, the theoretically predicted optimal paths were directly measured in Monte Carlo simulations which probe the distribution tails of $\mathcal{P}(H, T)$ with an importance sampling algorithm [24,25].

It was observed some time ago [15] that the OFM equations for Eq. (1) belong to a class of completely integrable classical systems. Recently this idea has borne fruit in Refs. [27,28] where the short-time large-deviation function of H was calculated exactly, for three major initial conditions, by combining the OFM with the Zakharov-Shabat inverse scattering method.

^{*}meerson@mail.huji.ac.il

[†]vilenkin@mail.huji.ac.il

The KPZ equation, however, is only one member of a whole family of continuum models of nonequilibrium stochastic interface growth. Since the beginning of the 1990s, several other models, with different mechanisms of nonlinearity and dissipation and different types of noise, have been proposed and studied, see Ref. [2] for an extensive review. We believe that the time is ripe to broaden the application range of the OFM by applying it to some of these systems. Here we focus on the Golubović-Bruinsma (GB) equation of stochastic interface growth [29]:

$$\partial_t h = -\nu \partial_x^4 h + \frac{\lambda}{2} (\partial_x h)^2 + \sqrt{D} \xi(x, t). \quad (3)$$

The GB equation retains the same nonlinearity and noise as in the KPZ equation (1), but it differs from the latter by the dissipation mechanism: Here it is surface diffusion, described by the fourth-derivative term $-\nu \partial_x^4 h$. In general, this difference is quite important as we will see shortly.

In the context of stochastic interface growth, the GB equation is a useful model equation [2,29], but the same equation also describes spatially extended one-dimensional nonequilibrium condensates in a variety of experimental settings, see Ref. [30] and references therein.

Without the nonlinear term, the GB equation (3) becomes the linear stochastic Mullins-Herring equation:

$$\partial_t h = -\nu \partial_x^4 h + \sqrt{D} \xi(x, t). \quad (4)$$

Its noiseless version $\partial_t h = -\nu \partial_x^4 h$, proposed by Mullins 65 years ago [31], describes the capillary relaxation of a solid surface, where the surface diffusion of adatoms is accompanied by adatom exchange between the surface and the bulk of the solid [32–36]. The linear stochastic equation (4) was introduced by Wolf and Villain [32] and by Das Sarma and Taborenea [37]. This equation and its analog with a conserved noise were extensively studied in the context of dynamic scaling behavior of interfaces [2,3,37–39]. Previously we employed the OFM to study the probability distribution $\mathcal{P}(H, T)$ of the one-point interface height for Eq. (4) with a conserved noise [40]. Here we study the short-time behavior of $\mathcal{P}(H, T)$ for the nonlinear GB equation (3). We suppose that the process starts at $t = 0$ from flat interface,

$$h(x, t = 0) = 0, \quad (5)$$

and condition the interface height at $x = 0$ on reaching a value H at time $t = T$ [41]:

$$h(x = 0, t = T) = H. \quad (6)$$

In the short-time limit, $T \ll T_{\text{NL}}$, where $T_{\text{NL}} = \nu^{5/7} (D\lambda^2)^{-4/7}$ is the characteristic nonlinear time of the GB equation, typical (that is, small) fluctuations of H are governed by the linear equation (4). As a result, they are Gaussian. Using the OFM, here we will obtain

$$-\ln \mathcal{P}(H, T) \simeq \frac{3\pi \nu^{1/4} H^2}{2^{3/4} \Gamma(1/4) D T^{3/4}}, \quad (7)$$

where $\Gamma(\dots)$ is the gamma function. As to be expected, Eq. (7) is in perfect agreement with previous results for the linear equation (4) [2,3,16].

Large deviations of H , corresponding to the tails of the distribution $\mathcal{P}(H, T)$, “feel” the presence of the nonlinear term

in the GB equation already at short times, and they demand a full account of the nonlinearity. As we show here, the tails of $\mathcal{P}(H, T)$ are non-Gaussian. For the upper tail $\lambda H \rightarrow +\infty$ we obtain a slower-than-Gaussian asymptotic

$$-\ln \mathcal{P}(H, T) \simeq \frac{\beta \nu^{1/3} H^{11/6}}{D |\lambda|^{11/6} T^{5/6}}, \quad (8)$$

where $\beta \simeq 1.73$. The asymptotic (8) is quite different from the short-time $\lambda H \rightarrow +\infty$ asymptotic of $\mathcal{P}(H, T)$ for the KPZ equation which scales as $-\ln \mathcal{P}(H, T) \sim H^{3/2} / T^{1/2}$ [10–13].

We also determine the lower tail, $\lambda H \rightarrow -\infty$, of $\mathcal{P}(H, T)$:

$$-\ln \mathcal{P}(H, T) \simeq \frac{8\sqrt{2|\lambda|} H^{5/2}}{15\pi D T^{1/2}}. \quad (9)$$

This faster-than-Gaussian tail coincides with the leading-order $\lambda H \rightarrow -\infty$ tail of $\mathcal{P}(H, T)$ for the KPZ equation [12,13]. This happens because the $\lambda H \rightarrow -\infty$ tail turns out to be independent of dissipation, be it the diffusion term of the KPZ equation or the surface-diffusion term of the GB equation.

Further, we obtain asymptotic solutions for the optimal paths of the system and compute the optimal paths numerically, using a modified version of the back-and-forth iteration algorithm developed by Chernykh and Stepanov [42,43]. The numerical solutions enable us to evaluate (of course, in a finite range of H) the complete large deviation function of height $s(H)$ [defined by Eq. (12) below] and verify our asymptotic results for the typical fluctuations and for the tails.

Here is a plan of the remainder of the paper. In Sec. II we present the OFM formulation (the equations and boundary conditions) for the evaluation of $\mathcal{P}(H, T)$ for Eq. (3). A derivation of the equations and boundary conditions is relegated to the Appendix. Section II also includes our numerical results for the complete $s(H)$. In Sec. III we present asymptotic solutions of the OFM problem in three different limits: $H \rightarrow 0$ (typical fluctuations), $\lambda H \rightarrow +\infty$ [the upper tail of $\mathcal{P}(H, T)$], and $\lambda H \rightarrow -\infty$ [the lower tail of $\mathcal{P}(H, T)$]. Our asymptotic solutions for the tails were motivated by the numerical results for the optimal paths in different regimes, and by expected analogies between the GB equation and the KPZ equation. Section IV contains a brief summary and a discussion of possible extensions of our results.

II. OFM FORMALISM

It is convenient to rescale the variables. After the rescaling transformation

$$\frac{t}{T} \rightarrow t, \quad \frac{x}{(\nu T)^{1/4}} \rightarrow x \quad \text{and} \quad \frac{|\lambda| T^{1/2} h}{\nu^{1/2}} \rightarrow h, \quad (10)$$

Eq. (3) becomes

$$\partial_t h = -\partial_x^4 h - \frac{1}{2} (\partial_x h)^2 + \sqrt{\epsilon} \xi(x, t), \quad (11)$$

where $\epsilon = D\lambda^2 T^{7/4} / \nu^{5/4}$, and we have assumed, without loss of generality, that $\lambda < 0$ [44]. Clearly, the exact distribution $\mathcal{P}(H, T)$ depends only on two dimensionless parameters: the rescaled height $\tilde{H} = |\lambda| T^{1/2} H / \nu^{1/2}$ and ϵ .

The OFM relies on a small parameter which justifies the saddle-point evaluation of the path integral. In the present case, we formally set $\epsilon \rightarrow 0$. In this asymptotic regime the weak-noise scaling holds:

$$-\ln \mathcal{P}(H, T) \simeq \frac{s(\tilde{H})}{\epsilon} = \frac{\nu^{5/4}}{D\lambda^2 T^{7/4}} s\left(\frac{|\lambda| T^{1/2} H}{\nu^{1/2}}\right), \quad (12)$$

and we will suppress the tilde in \tilde{H} in the following. The *a priori* unknown large deviation function $s(\dots)$ should be determined via minimization of the proper action functional, intrinsic in the saddle-point evaluation. The minimization procedure, outlined in the Appendix, yields an Euler-Lagrange equation which can be recast in a Hamiltonian form. The Hamilton's equations are

$$\partial_t h = -\partial_x^4 h - (1/2)(\partial_x h)^2 + \rho, \quad (13)$$

$$\partial_t \rho = \partial_x^4 \rho - \partial_x(\rho \partial_x h). \quad (14)$$

Their solution for $h(x, t)$, subject to proper boundary conditions, describe the optimal path, that is the most likely history of the interface $h(x, t)$, conditioned on H . In its turn, the conjugate momentum density field $\rho(x, t)$ describes (up to a rescaling) the most likely realization of the Gaussian white noise $\xi(x, t)$, conditioned on the same H .

The interface is initially flat, see Eq. (5). The “final” condition (6) can be temporarily incorporated via a Lagrange multiplier (see the Appendix), which leads to the boundary condition

$$\rho(x, t = 1) = \Lambda \delta(x), \quad (15)$$

where $\delta(\dots)$ is the delta function. The *a priori* unknown Lagrange multiplier Λ should be ultimately expressed through H .

Once the optimal path is determined, the rescaled action $s(H)$, which plays the role of the large deviation function of H , can be calculated from the equation

$$s(H) = \frac{1}{2} \int_0^1 dt \int_{-\infty}^{\infty} dx \rho^2(x, t). \quad (16)$$

Alternatively, $s(H)$ can be found from the “shortcut relation” $ds/dH = \Lambda$, which follows from the fact that H and Λ are conjugate variables, see, e.g., Ref. [45].

It is often convenient to rewrite Eqs. (13) and (14) in terms of the local interface slope $V(x, t) = \partial_x h(x, t)$:

$$\partial_t V + V \partial_x V = -\partial_x^4 V + \partial_x \rho, \quad (17)$$

$$\partial_t \rho + \partial_x(\rho V) = \partial_x^4 \rho. \quad (18)$$

Figure 1 shows the rescaled action $s(H)$, obtained by solving the OFM problem numerically with a modified back-and-forth iteration algorithm [42,43]. Evident in Fig. 1 is a strong asymmetry of the right and left tails of $\mathcal{P}(H, T)$.

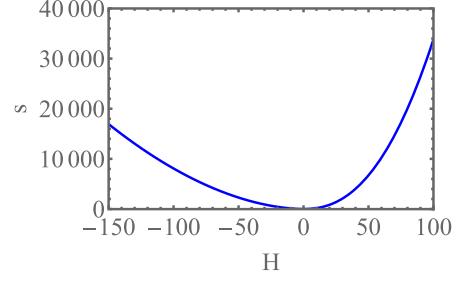


FIG. 1. The large-deviation function of the rescaled height $s(H)$, see Eq. (12), computed by solving the OFM equations (13) and (14) numerically with a modified back-and-forth iteration algorithm [42,43]. Evident is a strong asymmetry of the tails $H < 0$ and $H > 0$. To remind the reader, we set $\lambda < 0$.

III. ASYMPTOTICS OF $s(H)$

A. Typical fluctuations, $H \rightarrow 0$

Typical, small fluctuations of H are described by the limit of $H \rightarrow 0$ or $\Lambda \rightarrow 0$. In this limit we can drop the nonlinear terms in Eqs. (13) and (14) and obtain

$$\partial_t h = -\partial_x^4 h + \rho, \quad (19)$$

$$\partial_t \rho = \partial_x^4 \rho. \quad (20)$$

These linear equations provide the optimal fluctuation theory for Eq. (4), and they can be solved exactly. Solving Eq. (20) backward in time with the initial condition (15), we obtain

$$\rho(x, t) = \frac{\Lambda}{(1-t)^{1/4}} \Phi\left[\frac{x}{(1-t)^{1/4}}\right], \quad (21)$$

where

$$\Phi(z) = \frac{\Gamma(5/4)}{\pi} {}_0F_2\left(\frac{1}{2}, \frac{3}{4}; \frac{z^4}{256}\right) - \frac{\Gamma(3/4)}{8\pi} z^2 {}_0F_2\left(\frac{5}{4}, \frac{3}{2}; \frac{z^4}{256}\right), \quad (22)$$

and ${}_pF_q(a; b; z)$ is the generalized hypergeometric function [46]. This solution at different times is depicted on Fig. 2. It exhibits an oscillatory spatial decay, characteristic of the surface diffusion [31].

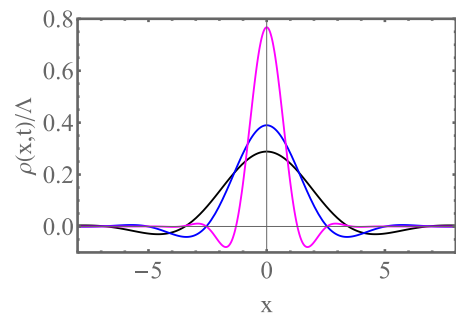


FIG. 2. The optimal history of rescaled noise $\rho(x, t)/\Lambda$ in the limit of small fluctuations, $H \rightarrow 0$, or $\Lambda \rightarrow 0$. Shown is the solution (21) at $t = 0$ (black), 0.7 (blue), and 0.85 (magenta).

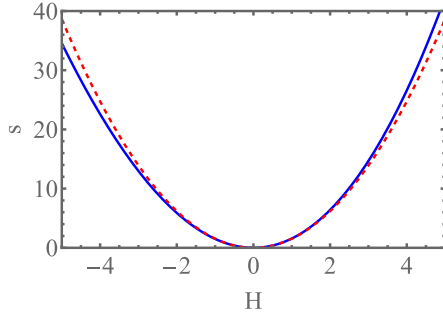


FIG. 3. The quadratic asymptotic (25) of $s(H)$ (dashed line) versus $s(H)$ found numerically (solid line). The numerical curve is a small fragment of the $s(H)$ curve from Fig. 1.

The action in terms of Λ can be obtained by substituting Eqs. (21) and (22) into Eq. (16):

$$s(\Lambda) = \frac{\Lambda^2}{2} \int_0^1 \frac{dt}{(1-t)^{1/4}} \int_{-\infty}^{\infty} dz \Phi^2(z) = \alpha \Lambda^2, \quad (23)$$

where $\alpha = \frac{\Gamma(1/4)}{6\sqrt{2\pi}} = 0.16174 \dots$. Now we have to express Λ through H . We can bypass the need to solve Eq. (19) by using “the shortcut relation” $ds/dH = \Lambda$. We have

$$\frac{ds}{dH} = \frac{ds}{d\Lambda} \frac{d\Lambda}{dH} = 2\alpha\Lambda \frac{d\Lambda}{dH} = \Lambda. \quad (24)$$

Therefore $\Lambda = H/2\alpha$, and we obtain the rescaled action

$$s(H \rightarrow 0) = \frac{H^2}{4\alpha}, \quad (25)$$

leading to Eq. (7) for $\mathcal{P}(H, T)$. Figure 3 compares the asymptotic (25) with the numerically computed $s(H)$, and a good agreement is observed for sufficiently small $|H|$. The Gaussian asymptotic (7), which predicts, in the original variables, a $T^{3/8}$ growth of the standard deviation of H with time T , perfectly agrees with the known results for Eq. (4), see page 142 of Ref. [2], Eq. (3.25) of Ref. [3], and Eq. (8) of Ref. [16]. Notice that the applicability condition of this asymptotic $|H| \ll 1$ in the rescaled variables depends on time T in the original variables:

$$|H| \ll \frac{\nu^{1/2}}{|\lambda|T^{1/2}}.$$

Therefore, when $T \rightarrow 0$ at fixed H , the Gaussian asymptotic is always valid. However, for a fixed T , this asymptotic breaks down for sufficiently large $|H|$, that is, in the distribution tails. Let us now describe these tails.

B. Upper tail: $\lambda H \rightarrow +\infty$

Our numerical simulations (see Fig. 4) show that the dominant contribution to the action in this tail comes from a solution of the type

$$h(x, t) = h_0(x) - ct \quad \text{and} \quad \rho(x, t) = \rho_0(x), \quad (26)$$

parametrized by c . In this solution the (rescaled) optimal realization of the noise $\rho(x, t)$ has the form of a stationary soliton of $\rho_0(x)$ which drives a traveling wave of $h(x, t)$ in the vertical direction with velocity c or, in the language of

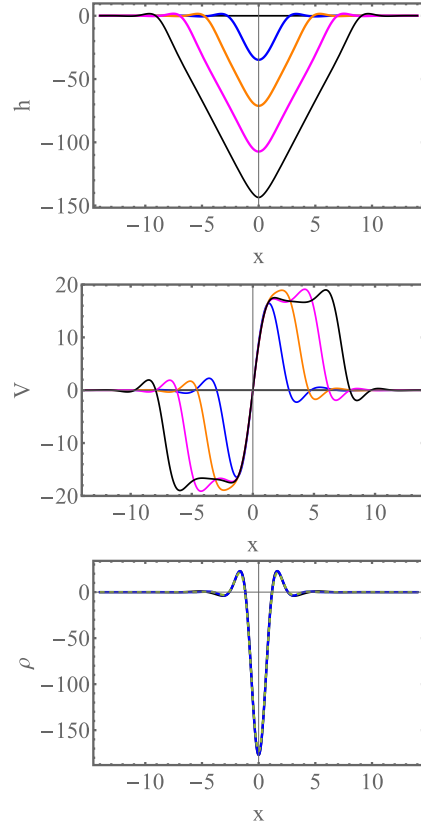


FIG. 4. The optimal path for large negative λH . Shown are $h(x, t)$ (top panel) and $V(x, t)$ (middle panel) obtained by solving numerically Eqs. (13) and (14) for $\Lambda = -200$ (which corresponds to $H \simeq -143.6$) at times $t = 0, 0.25, 0.5, 0.75,$ and 1 . The bottom panel shows $\rho(x, t)$ at times $t = 0.3, 0.6,$ and 0.9 . The V antishock, driven by a stationary ρ soliton, and two outgoing deterministic V shocks are clearly seen.

the slope $V = \partial_x V$, a stationary antishock $V(x, t) = V_0(x) \equiv h'_0(x) = 0$ located at $x = 0$. The ansatz (26) is the same as for the upper tail of $\mathcal{P}(H, T)$ for the KPZ equation [13], but the solution details are quite different. In particular, here the soliton-antishock solution exhibits decaying spatial oscillations. As $c \gg 1$ (indeed, in the leading order $c = |H| \gg 1$, see below), the soliton-antishock solution is strongly localized at $x = 0$. The V antishock does not satisfy the boundary conditions $V(|x| \rightarrow \infty) = 0$. Similarly to the KPZ equation, the remedy comes in the form of two outgoing deterministic (that is, $\rho = 0$) shocks of $V(x, t)$ which obey the equation

$$\partial_t V + V \partial_x V = -\partial_x^4 V \quad (27)$$

and satisfy the boundary conditions $V(x \rightarrow -\infty, t) = 2c$ and $V(x \rightarrow \infty, t) = 0$ for the right-moving shock and $V(x \rightarrow -\infty, t) = 0$ and $V(x \rightarrow \infty, t) = 2c$ for the left-moving shock.

Let us start with the soliton-antishock solution. Substituting the ansatz (26) into Eqs. (13) and (14) and integrating

one of the two resulting ordinary differential equations with respect to x , we obtain

$$\frac{d^3 V_0}{dx^3} = c - \frac{V_0^2}{2} + \rho_0, \quad (28)$$

$$\frac{d^3 \rho_0}{dx^3} = \rho_0 V_0, \quad (29)$$

where $V_0(x) = h'_0(x)$. The integration constant in Eq. (29) vanished because $\rho(|x| \rightarrow \infty, t) = 0$. After rescaling

$$z = (c/2)^{1/6} x, \quad v = (2c)^{-1/2} V_0, \quad r = (1/c) \rho_0 \quad (30)$$

we recast Eqs. (28) and (29) into a parameter-free form,

$$v'''(z) = 1 - v^2(z) + r(z), \quad (31)$$

$$r'''(z) = 2r(z)v(z), \quad (32)$$

where the primes denote the z derivatives. Remarkably, the rescaling transformation (30) already makes it possible to evaluate the rescaled action (16) for this tail up to a numerical constant $O(1)$ (which we will compute numerically). Using Eq. (30), we (i) go over from x and ρ to z and r in Eq. (16) and (ii) make use of the fact that, in the leading order, $\rho(x, t) = \rho_0(x)$ is time independent; see Eq. (26). We obtain

$$s \simeq \frac{1}{2} \int_{-\infty}^{\infty} dx \rho_0^2(x) = \beta c^{11/6} \simeq \beta |H|^{11/6}, \quad (33)$$

where

$$\beta = \frac{1}{2^{5/6}} \int_{-\infty}^{\infty} dz r^2(z), \quad (34)$$

and we also used the asymptotic relation

$$c \simeq h(x = 0, t = 1) = |H|,$$

see Eq. (26).

To compute the constant $\beta = O(1)$ from Eq. (34), we have to solve the ordinary differential equations (ODEs) (31) and (32). Analytical solution does not seem to be possible, so we solved these ODEs numerically. As $v(z)$ is antisymmetric, and $r(z)$ symmetric, with respect to $z \leftrightarrow -z$, it suffices to solve Eqs. (31) and (32) only for $z > 0$ with five boundary conditions $v(0) = v'(0) = r'(0) = 0$, $v(\infty) = 1$, and $r(\infty) = 0$. The resulting numerical solution for $v(z)$ and $r(z)$ is shown by dashed lines in Fig. 5. The functions $v(z)$ and $r(z)$ exhibit decaying oscillations. These can be easily understood from a linearization of Eqs. (31) and (32) around the asymptotic states $v = 1, r = 0$ at $z \rightarrow \infty$ and $v = -1$ and $r = 0$ at $z \rightarrow -\infty$. Finally, using the numerically found $r(z)$, we obtain from Eq. (34) $\beta \simeq 1.73$.

Figure 5 also shows, by solid lines, the V and ρ profiles obtained by solving numerically the full time-dependent OFM equations (17) and (18), using the modified back-and-forth iteration algorithm [42,43], for $\Lambda = -200$. The profiles were rescaled according to Eq. (30), with $c = |H| \simeq 143.6$. As one can see, the agreement is good. Because of the boundary conditions in time, Eqs. (6) and (15), the soliton-antishock solution breaks down at t close to 0 and 1. These narrow ‘‘boundary layers’’ in time, however, do not contribute to the action s in the leading order at $\lambda H \rightarrow +\infty$.

The upper panel of Fig. 6 shows that the asymptotic (33) with $\beta = 1.73$ rapidly converges to the numerical results at

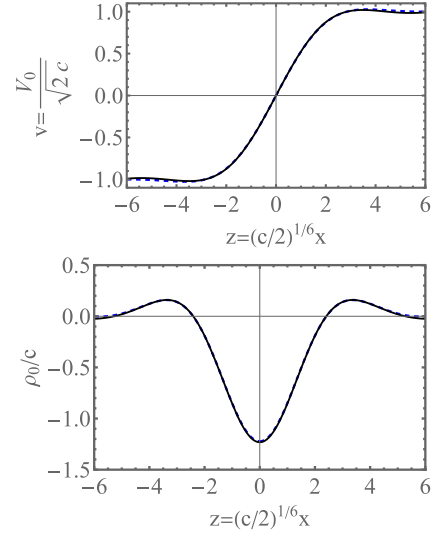


FIG. 5. The stationary soliton-antishock solution which dominates the upper tail $\lambda H \rightarrow +\infty$ of $\mathcal{P}(H, T)$. The dashed lines show a numerical solution of the ordinary equations (31) and (14) for the rescaled profiles $v(z)$ and $r(z)$. The solid lines show rescaled profiles $V(x, t = 0.5)$ and $\rho(x, t = 0.5)$, obtained by numerically solving the complete OFM equations (17) and (18) for $\Lambda = -200$.

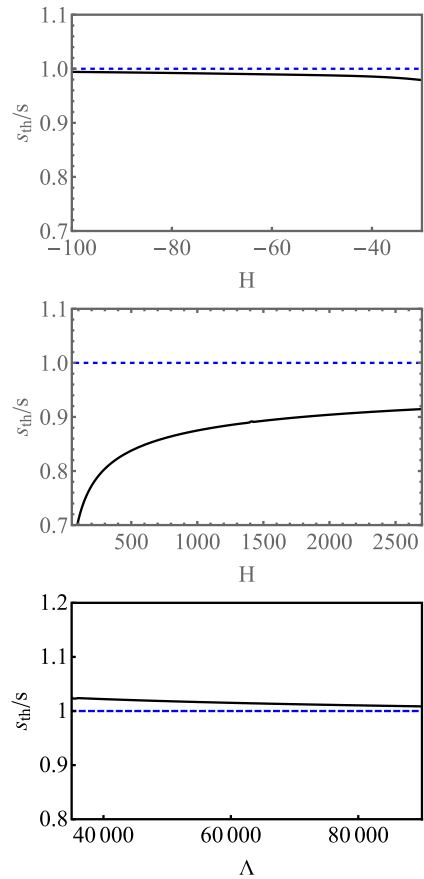


FIG. 6. Convergence of the asymptotics (33) (top) and (38) (middle and bottom) of the large-deviation function $s(H)$ to numerical results at large $|H|$ or $|\Lambda|$. Notice that the asymptotic (38) in terms of H (middle) converges much slower than the asymptotic $s(\Lambda) = (1/5)(3\pi/2)^{2/3} \Lambda^{5/3}$ in terms of Λ (bottom).

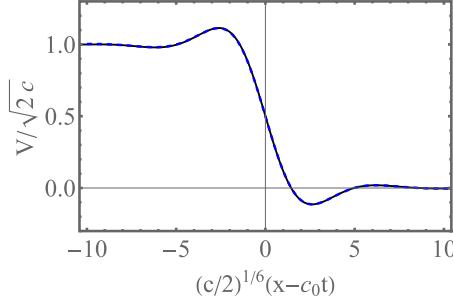


FIG. 7. Deterministic V shock: An intrinsic feature of the optimal path dominating the upper tail $\lambda H \rightarrow +\infty$ of $\mathcal{P}(H, T)$. Dashed line: Traveling front solution $V(x - c_0t)$ of Eq. (27). When properly rescaled, this solution obeys Eq. (35). Solid line: Rescaled profile $V(x, t = 0.9)$, obtained by numerically solving the complete OFM problem [Eqs. (17) and (18)] for $\Lambda = -200$. Here $c = |H| \simeq 143.6$ and $c_0 = \sqrt{|H|/2} \simeq 8.47$.

large negative H . In the original variables Eq. (33) yields the upper tail (8) of $\mathcal{P}(H, T)$.

To complete the solution for the optimal path, we now turn to the outgoing deterministic shock solutions which take care of the boundary conditions at large distances. These shocks do not contribute to the action, and they are described by traveling front solutions of the form $V(x, t) = F(x \pm c_0t)$ of Eq. (27). Equation (27) is a higher-order cousin of the Burgers equation $\partial_t V + V \partial_x V = \partial_x^2 V$. Because of the fourth-derivative dissipation term $-\partial_x^4 V$ the traveling shock of Eq. (27) exhibits decaying oscillations in space. However, exactly as in the case of the Burgers equation, the shock velocity c_0 is independent of the dissipation, and it is equal to $(V_+ + V_-)/2$, where V_+ and V_- are the asymptotic values of V in front of and behind the shock, respectively. For our right-moving shock $V_+ = 0$ and $V_- = \sqrt{2c}$ and vice versa for the left-moving shock. Therefore, the deterministic shock velocity $c_0 = \sqrt{c/2} \simeq \sqrt{|H|/2}$ turns out to be the same as for the KPZ equation [13,47].

The shock profiles, however, are markedly different from the KPZ case. In particular, they approach their respective constant values at $x = \pm\infty$ in an oscillatory manner. To compute the profiles we rescale $v = V/\sqrt{2c}$ and $z = (x/2)^{1/6}(x - c_0t)$ and solve the resulting parameter-free ODE,

$$v'''(z) = v(z) - v^2(z), \tag{35}$$

numerically. Since $v(z) - 1/2$ is an odd function of z , it suffices to solve Eq. (35) only for $z > 0$. For the right-moving shock the boundary conditions are $v(0) = 1/2$, $v''(0) = 0$, and $v(\infty) = 0$. The solution is shown by the dashed line in Fig. 7. The same figure shows, by the solid line, the properly rescaled V profiles obtained by solving the full time-dependent OFM equations (17) and (18) for $\Lambda = -200$. A good agreement is observed.

C. Lower tail: $\lambda H \rightarrow -\infty$

The lower tail has a very different nature from the upper one. As evidenced by our numerical solutions (see Fig. 8), in this limit the momentum density field $\rho(x, t)$ is large scale and therefore can be described by the *zero-dissipation*

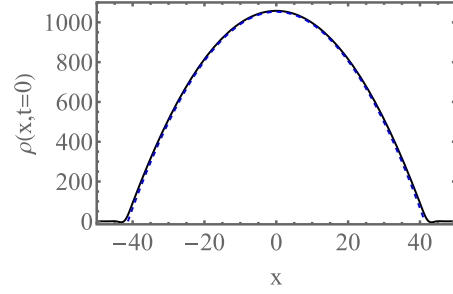


FIG. 8. Optimal configuration of the noise at $t = 0$ which dominates the lower tail $\lambda H \rightarrow -\infty$. Shown are the profiles of $\rho(x, t = 0)$, obtained numerically here (the solid line) and analytically in Ref. [13] (the dashed line), for $\Lambda = 58\,000$.

limit of Eqs. (17) and (18). This limit is obtained by dropping the fourth-derivative terms in Eqs. (17) and (18) which originate from the surface-diffusion term $-\nu \partial_x^4 h$ in the GB equation (11). The resulting ideal hydrodynamic equations,

$$\partial_t \rho + \partial_x(\rho V) = 0, \tag{36}$$

$$\partial_t V + V \partial_x V = \partial_x \rho, \tag{37}$$

coincide with those obtained for the lower tail of the KPZ equation [13]. This happens simply because the GB equation (11) and the KPZ equation (1) (and, as a result, the OFM equation for the two models) become identical in their respective zero-dissipation limits. As the boundary conditions at $t = 0$ and $t = 1$ are also the same for the two problems, this makes the solutions in the zero-dissipation limit identical as well.

Equations (36) and (37) describe an inviscid flow of an effective compressible gas with density ρ and velocity V , driven by the gradient of a *negative* pressure $P(\rho) = -\rho^2/2$. The negative pressure causes collapse of the whole gas into the origin at $t = 1$, in compliance with the boundary condition (15). This idealized problem turns out to be exactly soluble, and its solution was obtained in Ref. [13], see also Ref. [12]. The spatial profile of $\rho(x, t)$ is parabolic in x at all times, and it lives on a compact support which shrinks to zero at $t = 1$. The spatial profile of $V(x, t)$ includes two regions. In the internal region, which has the same compact support as $\rho(x, t)$, the V profile is linear in x . In the external region $V(x, t)$ comes from the solution of the Hopf equation $\partial_t V + V \partial_x V = 0$ and its matching with the internal solution [13]. We checked that this analytical solution agrees very well with the numerical solution of the full system of Eqs. (17) and (18), which describe the optimal path of the GB interface. As an example, Fig. 8 shows $\rho(x, t = 0)$, obtained numerically for $\Lambda = 58\,000$, and the corresponding theoretical profile of $\rho(x, t = 0)$ —a parabola—obtained in Ref. [13].

The final result for the rescaled action $s(H)$ in this regime is

$$s(H \rightarrow \infty) = \frac{8\sqrt{2}}{15\pi} H^{5/2}, \tag{38}$$

the same as for the KPZ equation [12,13]. In the original variables, Eq. (38) leads to the announced lower tail (9) of $\mathcal{P}(H, T)$. The middle panel of Fig. 6 shows that the asymptotic (38) slowly converges to the numerical result

at large positive H . The slow convergence signals the presence of a relatively large subleading term in Eq. (38) which is not captured by the leading-order hydrodynamic solution. Our numerical data are compatible with a subleading term $O(H^2 \ln H)$. The bottom panel of Fig. 6 shows a much faster convergence of the same asymptotic (38) but rewritten in terms of the Lagrange multiplier Λ : $s(\Lambda \rightarrow \infty) = (1/5)(3\pi/2)^{2/3} \Lambda^{5/3}$ [13].

IV. SUMMARY AND DISCUSSION

We studied large deviations of the one-point height, as described by the probability distribution $\mathcal{P}(H, T)$, of an initially flat interface, governed by the GB equation (3). We focused on the short-time limit. Employing the OFM, we addressed both typical fluctuations, see Eq. (7), and the distribution tails (8) and (9). The lower tail (9) coincides with its counterpart for the KPZ equation. The universal character of this tail is explained by the macroscopic character of the optimal realization of noise in this regime. On large scales one can neglect dissipation of *any* origin if it is described by a differential operator of a higher than first order, be it diffusion, surface diffusion, and so on.

The upper tail (8) turns out to be very different both from its counterpart for the KPZ equation and from the higher tail (8). The reason is that the optimal realization of the noise represents a strongly localized soliton of ρ , see Eqs. (26) and (30). The soliton width scales as $H^{-1/6} \ll 1$. At such small scales the dissipation is as important as the nonlinearity. Since the dissipation term in the GB equation (the surface diffusion) is different from that in the KPZ equation (the ordinary diffusion), the resulting tails are also different.

Importantly, the optimal paths of the interface in this problem respect, for all H , the mirror symmetry, $h(-x, t) = h(x, t)$, $V(-x, t) = -V(x, t)$, and $\rho(-x, t) = \rho(x, t)$. There are two important consequences of this symmetry. The first consequence is that, in analogy with the KPZ equation [13,14], the upper tail $\lambda H \rightarrow +\infty$ of $\mathcal{P}(H, T)$, see Eq. (8), should be universal for a whole class of deterministic initial conditions. The reason is that the ρ soliton and V antishock are strongly localized at $x = 0$, while two expanding deterministic shocks make it possible to match the small soliton-antishock region with macroscopic external regions. The deterministic shocks can accommodate any problem-specific boundary conditions, and they do not contribute to the action in the leading order.

The second consequence of the mirror symmetry of the optimal paths comes in the form of a simple connection between the action $s(H)$, corresponding to $\mathcal{P}(H, T)$ for the infinite interface $|x| < \infty$ and the action $s_{1/2}(H)$, corresponding to $\mathcal{P}(H, T)$ for the half-infinite interface $0 \leq x < \infty$ with a reflecting wall at $x = 0$. Indeed, exploiting the mirror symmetry, we obtain

$$s_{1/2}(H) = \frac{1}{2} \int_0^1 dt \int_0^\infty dx \rho^2(x, t) = \frac{s(H)}{2}, \quad (39)$$

for any H . That is, the probability of observing a certain value of H in the half-infinite system is always higher than in the infinite system, and it becomes *exponentially* higher in the

tails. The same property is observed for the KPZ equation for all deterministic initial conditions [18].

It would be interesting to use the OFM for the evaluation of the probability distribution $\mathcal{P}(H, T)$ of the one-point height H in higher dimensions. There is a technical subtlety here: The short-time variance of $\mathcal{P}(H, T)$ —which is controlled by the d -dimensional version of the linear equation (4)—is well defined only at $d < 4$, while at $d \geq 4$ it diverges [3,16,48]. A remedy to this divergence involves regularization, either by introducing small but finite spatial correlations of the noise [3] or studying the interface height averaged over a small ball around the origin rather than the strictly one-point height H [16]. However, in the GB equation it remains well defined (and does not require a regularization) in the experimentally relevant dimensions $d = 2$ and 3 , so one can proceed to studying $\mathcal{P}(H, T)$. In d dimensions the GB equation, rescaled according to Eq. (10), acquires the following form:

$$\partial_t h = -\nabla^4 h - \frac{1}{2}(\nabla h)^2 + \sqrt{\epsilon_d} \xi(\mathbf{x}, t), \quad (40)$$

where we have again assumed, without loss of generality, that $\lambda < 0$. In Eq. (40)

$$\epsilon_d = \frac{DT^{\frac{8-d}{4}} \lambda^2}{\nu^{\frac{d+4}{4}}} = \left(\frac{T}{T_{\text{NL}}} \right)^{\frac{8-d}{4}}, \quad (41)$$

where

$$T_{\text{NL}} = \frac{\nu^{\frac{d+4}{8-d}}}{D^{\frac{4}{8-d}} |\lambda|^{\frac{8}{8-d}}} \quad (42)$$

is the characteristic nonlinear time. Equation (41) implies that, at short times, the parameter ϵ_d is small and, as a result, the OFM is applicable in the experimentally relevant dimensions $d = 2$ and 3 .

ACKNOWLEDGMENTS

We are grateful to I. Amelio for pointing out to us Ref. [30] and for a useful discussion, and to N. R. Smith for advice. B.M. acknowledges support from the Israel Science Foundation (ISF) through Grant No. 1499/20.

APPENDIX: DERIVATION OF THE OFM EQUATIONS (13)–(15)

Derivation of Eqs. (13)–(15) closely follows that for the KPZ equation (1), see, e.g., Ref. [13]. Using Eq. (3), we can express the Gaussian noise term as

$$\sqrt{D} \xi(x, t) = \partial_t h + \nu \partial_x^4 h - \frac{\lambda}{2} (\partial_x h)^2. \quad (A1)$$

The corresponding Gaussian action is equal to S/D , where

$$S = \frac{1}{2} \int_0^T dt \int_{-\infty}^{\infty} dx \left[\partial_t h + \nu \partial_x^4 h - \frac{\lambda}{2} (\partial_x h)^2 \right]^2. \quad (A2)$$

The OFM involves minimization of this action with respect to the interface height histories $h(x, t)$, subject to the conditions (5) and (6). The linear variation of the action is

$$\delta S = \int_0^T dt \int_{-L/2}^{L/2} dx \left[\partial_t h + \nu \partial_x^4 h - \frac{\lambda}{2} (\partial_x h)^2 \right] \times (\partial_x \delta h + \nu \partial_x^4 \delta h - \lambda \partial_x h \partial_x \delta h). \quad (A3)$$

Let us introduce the effective momentum density field $\rho(x, t) = \delta L / \delta v$, where $v \equiv \partial_t h$, and

$$L\{h\} = \frac{1}{2} \int_{-\infty}^{\infty} dx \left[\partial_t h + v \partial_x^4 h - \frac{\lambda}{2} (\partial_x h)^2 \right]^2 \quad (\text{A4})$$

is the Lagrangian: a functional of $h(x, t)$. The effective momentum density field describes the optimal realization of the noise. We obtain

$$\rho = \partial_t h + v \partial_x^4 h - \frac{\lambda}{2} (\partial_x h)^2, \quad (\text{A5})$$

and arrive at

$$\partial_t h = -v \partial_x^4 h + \frac{\lambda}{2} (\partial_x h)^2 + \rho, \quad (\text{A6})$$

the first of the two Hamilton equations of the OFM. Now we can rewrite the linear variation (A3) as

$$\delta S = \int_0^T dt \int_{-\infty}^{\infty} dx \rho (\partial_t \delta h + v \partial_x^4 \delta h - \lambda \partial_x h \partial_x \delta h). \quad (\text{A7})$$

After several integrations by parts we obtain the Euler-Lagrange equation, which yields the second Hamilton's equation:

$$\partial_t \rho = v \partial_x^4 \rho + \lambda \partial_x (\rho \partial_x h). \quad (\text{A8})$$

The boundary terms in space, resulting from the integrations by parts, all vanish because of the boundary conditions at $|x| \rightarrow \infty$. There are, however, two boundary terms in time,

at $t = 0$ and $t = T$, which result from the integration by part of the first term under the double integral in Eq. (A7). The term $\int dx \rho(x, 0) \delta h(x, 0)$ vanishes because the height profile at $t = 0$ is specified by Eq. (5). Then boundary term $\int dx \rho(x, T) \delta h(x, T)$ must also vanish. Since we specified $h(x, T)$ at $x = 0$, the variation of h at this point must vanish: $\delta h(x = 0, T) = 0$. However, $\rho(x = 0, T)$ can be arbitrary. On the other hand, $h(x \neq 0, T)$ is not specified; therefore $\rho(x \neq 0, T)$ must vanish. To determine the exact form of the boundary condition at $t = T$, we accommodate the constraint $h(0, T) = H$ by adding the term

$$\Lambda h(0, T) = \Lambda \int_{-L}^L \delta(x) h(x, T) dx, \quad (\text{A9})$$

to the action, where Λ is a Lagrange multiplier [18]. As a result, the boundary term of δS at $t = T$ becomes $\int dx [\rho(x, T) - \Lambda \delta(x)] \delta h(x, T)$, which leads to the boundary condition [10,13]

$$\rho(x, T) = \Lambda \delta(x). \quad (\text{A10})$$

Λ is ultimately set up by the condition $h(x = 0, T) = H$.

Performing the rescaling, described in Eq. (10), and introducing the rescaled momentum density field, $|\lambda| T^{3/2} v^{-1/2} \rho \rightarrow \rho$, we bring Eqs. (A6), (A8), and (A10) to the forms (13), (14), and (15), respectively (with a rescaled Λ).

Finally, Eqs. (16) of the main text follows from Eqs. (A2) and (A5).

-
- [1] T. Vicsek, *Fractal Growth Phenomena* (World Scientific, Singapore, 1992).
- [2] A.-L. Barabasi and H. E. Stanley, *Fractal Concepts in Surface Growth* (Cambridge University Press, Cambridge, UK, 1995).
- [3] J. Krug, *Adv. Phys.* **46**, 139 (1997).
- [4] M. Kardar, G. Parisi, and Y.-C. Zhang, *Phys. Rev. Lett.* **56**, 889 (1986).
- [5] T. Halpin-Healy and Y.-C. Zhang, *Phys. Rep.* **254**, 215 (1995); T. Halpin-Healy and K. A. Takeuchi, *J. Stat. Phys.* **160**, 794 (2015).
- [6] I. Corwin, *Random Matrices: Theory Appl.* **01**, 1130001 (2012).
- [7] J. Quastel and H. Spohn, *J. Stat. Phys.* **160**, 965 (2015).
- [8] H. Spohn, in *Stochastic Processes and Random Matrices: Lecture Notes of the Les Houches Summer School*, Vol. 104, edited by G. Schehr, A. Altland, Y. V. Fyodorov and L. F. Cugliandolo (Oxford University Press, Oxford, UK, 2015), arXiv:1601.00499.
- [9] K. A. Takeuchi, *Physica A* **504**, 77 (2018).
- [10] I. V. Kolokolov and S. E. Korshunov, *Phys. Rev. B* **75**, 140201(R) (2007).
- [11] I. V. Kolokolov and S. E. Korshunov, *Phys. Rev. B* **78**, 024206 (2008).
- [12] I. V. Kolokolov and S. E. Korshunov, *Phys. Rev. E* **80**, 031107 (2009).
- [13] B. Meerson, E. Katzav, and A. Vilenkin, *Phys. Rev. Lett.* **116**, 070601 (2016).
- [14] A. Kamenev, B. Meerson, and P. V. Sasorov, *Phys. Rev. E* **94**, 032108 (2016).
- [15] M. Janas, A. Kamenev, and B. Meerson, *Phys. Rev. E* **94**, 032133 (2016).
- [16] N. R. Smith, B. Meerson, and P. V. Sasorov, *Phys. Rev. E* **95**, 012134 (2017).
- [17] B. Meerson and J. Schmidt, *J. Stat. Mech.* (2017) 103207.
- [18] N. R. Smith, B. Meerson, and P. V. Sasorov, *J. Stat. Mech.* (2018) 023202.
- [19] N. R. Smith, A. Kamenev, and B. Meerson, *Phys. Rev. E* **97**, 042130 (2018).
- [20] N. R. Smith and B. Meerson, *Phys. Rev. E* **97**, 052110 (2018).
- [21] B. Meerson and A. Vilenkin, *Phys. Rev. E* **98**, 032145 (2018).
- [22] T. Asida, E. Livne, and B. Meerson, *Phys. Rev. E* **99**, 042132 (2019).
- [23] N. R. Smith, B. Meerson, and A. Vilenkin, *J. Stat. Mech.* (2019) 053207.
- [24] A. K. Hartmann, B. Meerson, and P. Sasorov, *Phys. Rev. Res.* **1**, 032043(R) (2019).
- [25] A. K. Hartmann, B. Meerson, and P. Sasorov, *Phys. Rev. E* **104**, 054125 (2021).
- [26] N. Smith, *Phys. Rev. E* **106**, 044111 (2022).
- [27] A. Krajenbrink and P. Le Doussal, *Phys. Rev. Lett.* **127**, 064101 (2021).
- [28] A. Krajenbrink and P. Le Doussal, *Phys. Rev. E* **105**, 054142 (2022).
- [29] L. Golubović and R. Bruinsma, *Phys. Rev. Lett.* **66**, 321 (1991).
- [30] I. Amelio, A. Chiocchetta, and I. Carusotto, arXiv:2303.03275.

- [31] W. W. Mullins, *J. Appl. Phys.* **28**, 333 (1957); in *Metal Surfaces: Structure, Energetics and Kinetics*, edited by W. D. Robertson and N. A. Gjostein (American Society of Metals, Metals Park, OH, 1963), p. 17.
- [32] D. E. Wolf and J. Villain, *Europhys. Lett.* **13**, 389 (1990).
- [33] J. Villain, *J. Phys. I France* **1**, 19 (1991).
- [34] C. N. Luse and A. Zangwill, *Phys. Rev. B* **48**, 1970 (1993).
- [35] J. W. Cahn and J. E. Taylor, *Acta Metall. Mater.* **42**, 1045 (1994).
- [36] A. J. Vilenkin and A. Brokman, *Phys. Rev. B* **56**, 9871 (1997).
- [37] S. Das Sarma and P. Tamborenea, *Phys. Rev. Lett.* **66**, 325 (1991).
- [38] Z. Rácz, M. Siegert, D. Liu, and M. Plischke, *Phys. Rev. A* **43**, 5275 (1991).
- [39] M. Siegert and M. Plischke, *Phys. Rev. Lett.* **68**, 2035 (1992).
- [40] B. Meerson and A. Vilenkin, *Phys. Rev. E* **93**, 020102(R) (2016); **93**, 059901(E) (2016).
- [41] Similarly to the KPZ equation [8], the solution of Eq. (3) must include a systematic interface motion, caused by the rectification of the noise by the (sign-definite) nonlinearity. Our H is defined in a moving frame, where this systematic motion is subtracted.
- [42] A. I. Chernykh and M. G. Stepanov, *Phys. Rev. E* **64**, 026306 (2001).
- [43] We implemented a modified version of the back-and-forth iteration algorithm [42], as described in Ref. [49]. The implementation of this algorithm involves an implicit finite-difference scheme. In the present case the Thomas algorithm for solving linear algebraic equations, intrinsic in the finite-difference method (see, e.g., Ref. [50]), had to be modified to accommodate pentadiagonal matrices, which arise due to the fourth-order spatial derivatives in Eqs. (13) and (14). The ordinary differential equations, which appear in Sec. III B, were solved using standard tools of Mathematica.
- [44] Indeed, changing λ to $-\lambda$ is equivalent to changing h to $-h$.
- [45] F. D. Cunden, P. Facchi, and P. Vivo, *J. Phys. A: Math. Theor.* **49**, 135202 (2016).
- [46] Wolfram Research, Inc., Mathematica, Version 13.2, Champaign, IL (2022).
- [47] Since $c_0 \simeq \sqrt{|H|/2} \gg 1$, the characteristic width of the outgoing shocks is much smaller than the distance $\simeq |H|$ each of them travels until $t = 1$. Therefore, at large scales the shocks can be described by the zero-dissipation Hopf equation $\partial_t V + V \partial_x V = 0$.
- [48] For the KPZ equation the one-point-height variance at short times is described by the Edwards-Wilkinson equation $\partial_t h = \nu \partial_x^2 h + \sqrt{D} \xi(x, t)$, and it requires regularization already at $d \geq 2$ [3,16].
- [49] B. Meerson, A. Vilenkin, and P. L. Krapivsky, *Phys. Rev. E* **90**, 022120 (2014).
- [50] A. A. Samarskii and E. S. Nikolaev, *Numerical Methods for Grid Equations*, Vols. I and II (Birkhäuser, Basel, 1989).